

Experimental Investigations on Solidification of 500-kg Steel Ingots with Laboratory Trials



ZHIYE CHEN, DIETER SENK, and FELIX FIRSBACH

The present work focuses on the solidification process of large steel ingots. Several complex solidification phenomena in large ingots were investigated by means of experimental hot modeling and cold modeling. In hot modeling, a 500 kg ingot solidified slowly in a specially insulated mold and this slow solidification process simulates the solidification of industrial scale ingots with a weight between 3 and 6 t. Temperature was measured by thermocouples during solidification and curves were plotted, and as-cast structure and macrosegregation of alloying elements were quantified. The A segregates were produced in the laboratory hot trials and quantitatively investigated. Meanwhile, water modeling (cold modeling) using NH_4Cl solution was conducted with different cooling/heating conditions. Macroscopic crystal growth phenomena, such as dendritic growth, sedimentation of crystals, and convective fluid flow, were directly observed and analyzed, and flow channels were also observed and compared with A segregates in the hot modeling.

<https://doi.org/10.1007/s11663-018-1325-5>

© The Minerals, Metals & Materials Society and ASM International 2018

I. INTRODUCTION

SOLIDIFICATION in large steel ingots and upcoming large continuous cast (CC) semiproducts is an important but not completely understood phenomenon. Due to the extremely long solidification time in large cast products, *e.g.*, up to 24 hours, the solidification behavior is different from ingots or CC products with common cross sections. For example, melt flow plays a more important role in solidification in larger ingots. Due to the long solidification time and the ingot scale, thermal and solutal convective flow are more intensive in both mesoscopic and macroscopic scales; local remelting could happen and stimulate the instable channel formation; free crystals settle down and interact with the local melt flow; and, as a result, the as-cast structure of large ingots will be different from those in small ingots and CC products, especially regarding the geometrical intensity of meso- and macrosegregation.

Nowadays, there is a tendency to produce extremely large ingots over 600 t^[1–3] and continuous cast slabs with a thickness over 500 mm^[4] that are round with a dimension over 900 mm.^[5] In 2009, the China National Erzhong Group produced a 560 t ingot,^[1] and in the

same year, China First Heavy Industries cast an ingot with the weight of 580 t.^[2] In 2012, Japan Steel Works produced two ingots with weights of 650 and 670 t, which were the largest ingots in the world at that time.^[3] The main application of the heavy ingots and continuous cast slabs are retaining components such as reaction vessels for nuclear power plants and rotating components such as drive shafts of gas turbines and generator rotors.^[6] These high value products demand high quality of the as-cast semiproducts, and the production of the heavy steel semiproducts with adequate control of the quality becomes one of the great concerns for steelmakers worldwide.

Studies on heavy ingot casting and continuous casting with large cross sections were started in the 1960s.^[7–11] Plenty of studies on ingot macrostructure and macrosegregation with various ingot size and weight were conducted, mainly in terms of as-cast structure and carbon segregation degree along the centerline of the ingot.^[12–17] For example, A and V segregates were investigated in ingots with weights from 30 to 300 t by using sulfur printing and macroetching methods.^[8,11]

In the recent two decades, numerous modeling approaches were widely applied for the simulation of ingot solidification and the prediction of macrosegregation as well as solidification structure.^[18–24] However, among these works, few experimental studies were reported on the solidification of large ingots, especially quantitative investigation on A segregation, as-cast macrostructure, and temperature evolution during the solidification process.^[8,22] Due to the lack of quantitative experimental data, fundamental knowledge and

ZHIYE CHEN, DIETER SENK, and FELIX FIRSBACH are with the Department of Ferrous Metallurgy, RWTH Aachen University, 57072 Aachen, Germany. Contact e-mail: zhiye.chen@rwth-aachen.de

Manuscript submitted July 15, 2017.

Article published online July 19, 2018.

deep understanding of basic macroscopic solidification phenomena are still missing, such as the mechanism of A segregation, sedimentation, and growth of free crystals, convective fluid flow during solidification, and the solute redistribution on the microscopic solid/liquid interface during solidification and remelting. Furthermore, numerical simulation of ingot solidification cannot be validated efficiently without enough experimental work, since numerical models are based on a couple of macroscopic and microscopic mathematical models, such as the local solute redistribution equation model, which considers the interdendritic fluid flow and the movement of isotherms,^[10] the continuum models based on mixture theory,^[23] and the volume averaged models, which couple the microscopic interaction between different phases and the macroscopic system strongly together.^[20,24] These models are based on the understanding of the physical phenomena of solidification, and the understanding of physical phenomena demands adequate experimental data in different scales.

The current research attempts to investigate and model the complex macroscopic solidification phenomena in large steel ingots experimentally. On one hand, a special insulating mold was built of refractory bricks and insulating materials for ingot casting trials with the cast weight of 500 kg. The ingot solidification process is slowed by insulation, the solidification time is prolonged, and several complex phenomena, such as sedimentation of equiaxed grains and remelting, took place. Through these hot trails, the solidification of industrial scale ingots with weight of several tons can be simulated, which is called “hot modeling.” On the other hand, water modeling experiments (“cold modeling”) were conducted by using NH₄Cl salt-in-water solution as a transparent analog to gain insight into the ingot solidification. The aim of this work is to prepare a comprehensive set of models for the solidification of steel ingots by laboratory experiments to attain deeper understanding of the ingot solidification process and to provide experimental data for the validation of numerical simulation.

II. EXPERIMENTS: HOT MODELING

The steel grade used in the present study is a high-carbon low-alloy steel (Table I). In order to obtain the target composition, online measurement was carried out during melting. For each casting trial, at least one-disc Minco immersion sample was taken from the melt in the open furnace by a glass suction sampler. The composition of the disc samples was quickly analyzed

with the help of the pulse discrimination analyzer by optical emission spectrometry (PDA-OES). Based on the measured composition, a certain amount of alloying elements were added into the melt to adjust the final composition of the melt. Sulfur powder was also added to obtain the aim [S] content between 0.01 and 0.02 wt pct for the subsequent macrostructure characterization by sulfur printing.

The mold for the 500-kg ingot casting hot trials was specially designed to withstand the ferrostatic pressure of the steel melt at higher than 1400 °C for several hours. Three layers of refractory and insulating materials with thermal conductivity between 0.19 and 1.85 W/mK and different strength were cemented to each other and then integrated in a square-shaped steel box with its width and height about 1 m each, as shown in Figure 1(a). The mold is slightly tapered for stripping after solidification. The total thickness of the refractory bricks and insulating material of the mold is 300 mm, and a mold cover with thickness of 300 mm covers the mold cavity. During casting experiments, steel melt was tapped from the open furnace into a runner and the melt flew from the runner through a ceramic casting tube into the mold, as shown in Figure 1(b).

Directly after pouring, approximately 2 kg of insulating rice husk ashes were added through the casting tubes into the mold to protect the melt from heat loss at the top. Exothermic hot-top plates were cemented by refractory mortar onto the inner wall of the mold at the upper part to create the hot-top condition (shown in Figure 2). Two thermocouples (type S) were integrated into the mold cavity from the top of the mold to measure the ingot inner temperature. As Figure 2 shows, both thermocouples were inserted from the top at the ingot height of 350 mm and are 25 and 100 mm from the ingot centerline, respectively. The thermocouples were protected by quartz glass inner tubes (7 mm outer diameter, 1 mm wall thickness) and Cermotherm outer tubes (ceramic metal, 60 pct Mo-40 pct ZrO₂)^[25] with an outer diameter of 20 mm and a wall thickness of 6.5 mm against chemical and mechanical impact. Pouring started from the induction furnace at $T_{\text{pouring}} = 1594$ °C of a superheat of 124 K.

After the 500 kg ingot was completely solidified and cooled for 48 hours, the ingot was stripped out from the top of the mold. After cooling to room temperature, the ingot was delivered to steelwork AG der Dillinger Hüttenwerk to be sawed with a band saw. Samples were taken from the longitudinal and transverse cross sections of the ingot, and the as-cast macrostructure was revealed by macroetching and sulfur printing. The microstructure was analyzed with regard to dendrite

Table I. Chemical Composition of the High-Carbon Low-Alloy Steel, Al-Killed, $T_{\text{solidus}} = 1348$ °C, and $T_{\text{liquidus}} = 1470$ °C

Element	C	Al	Si	P	S	Mn
Percent (Wt Pct)	0.538	0.030	0.378	< 0.01	0.01 to 0.02	0.538

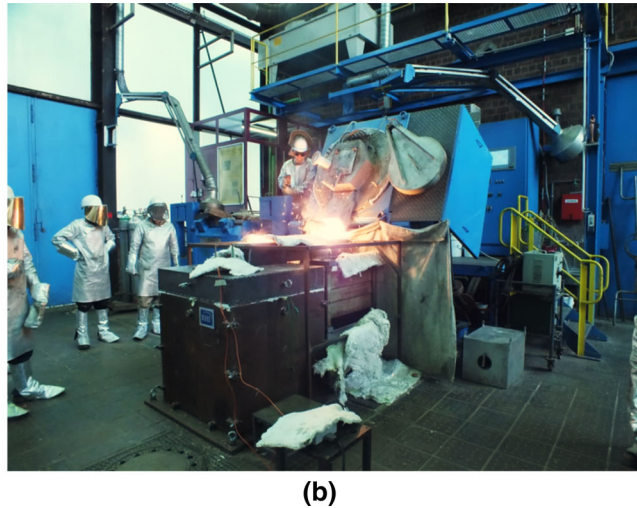
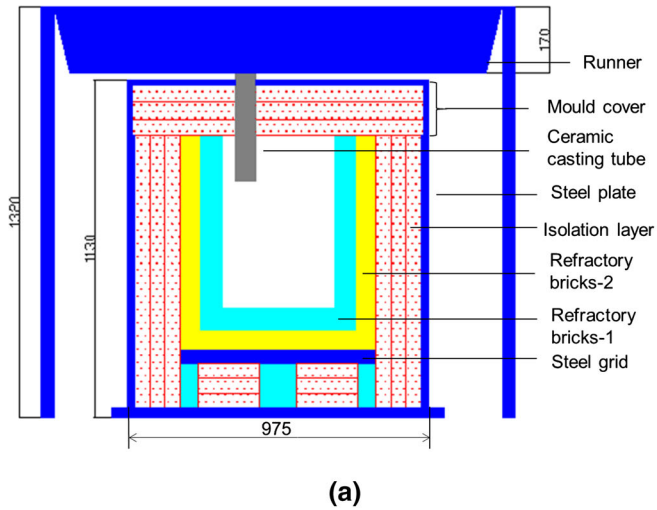


Fig. 1—(a) Schematic illustration of the mold and the tundish for the 500-kg ingot (side view) and (b) casting of the 500-kg ingot at IEHK, RWTH Aachen University.

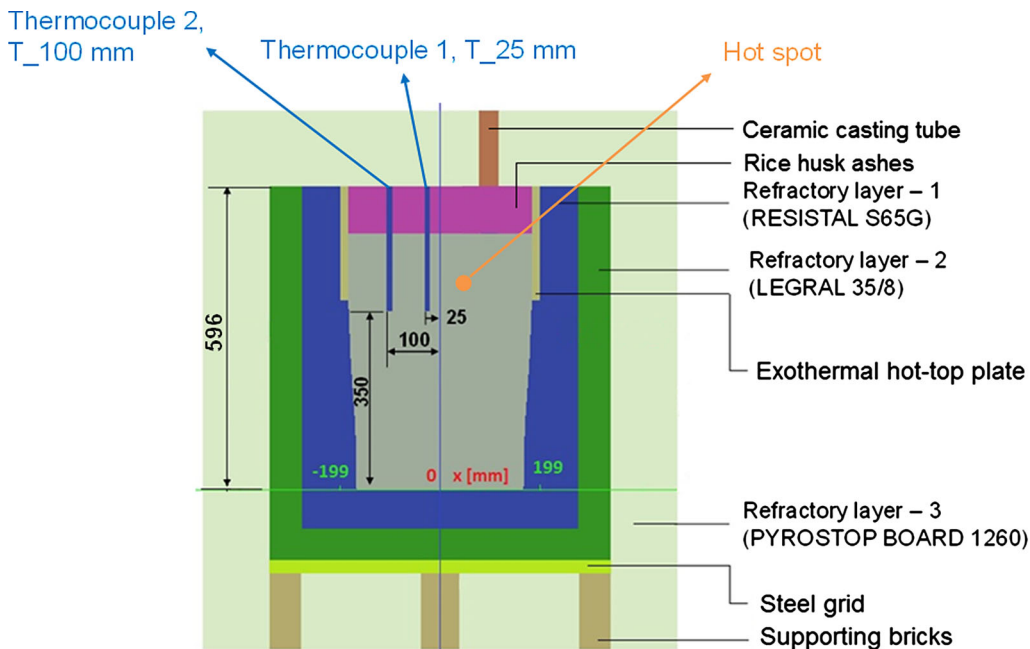


Fig. 2—Thermocouples in the ingot; view cut in ingot center plane.

arm spacing, macrosegregation of alloying elements were quantified with the help of PDA-OES, and mesosegregation-like A segregates were investigated quantitatively with electron microprobe analysis. The results are presented and discussed in Section IV.

III. EXPERIMENTS: COLD MODELING

Since there is great similarity between crystallization of a salt-water system and metal solidification regarding dendritic growth, sedimentation of free crystals, as well as convective flow, cold modeling using NH_4Cl aqueous solution was applied for the observation of a few macroscopic solidification phenomena.

In the present study, a quasi-two-dimensional square-shaped mold was built up with glass plates (front and back) for optical observation and aluminum plates (at left and right sides) for good thermal conduction as well as a Plexiglass plate (at the bottom) for thermal insulation, as illustrated in Figure 3. The inner dimension of the water model is 130 mm in width, 210 mm in height, and 18 mm in thickness. The water model can be cooled or heated through the aluminum plates at both sides. NH_4Cl aqueous solution was heated until NH_4Cl was completely dissolved and then poured into the mold. In the present study, saturated solution with the NH_4Cl concentration of 35.6 wt pct at 60 °C was used. The temperature and the concentration of the NH_4Cl solution were chosen based on the consideration that,

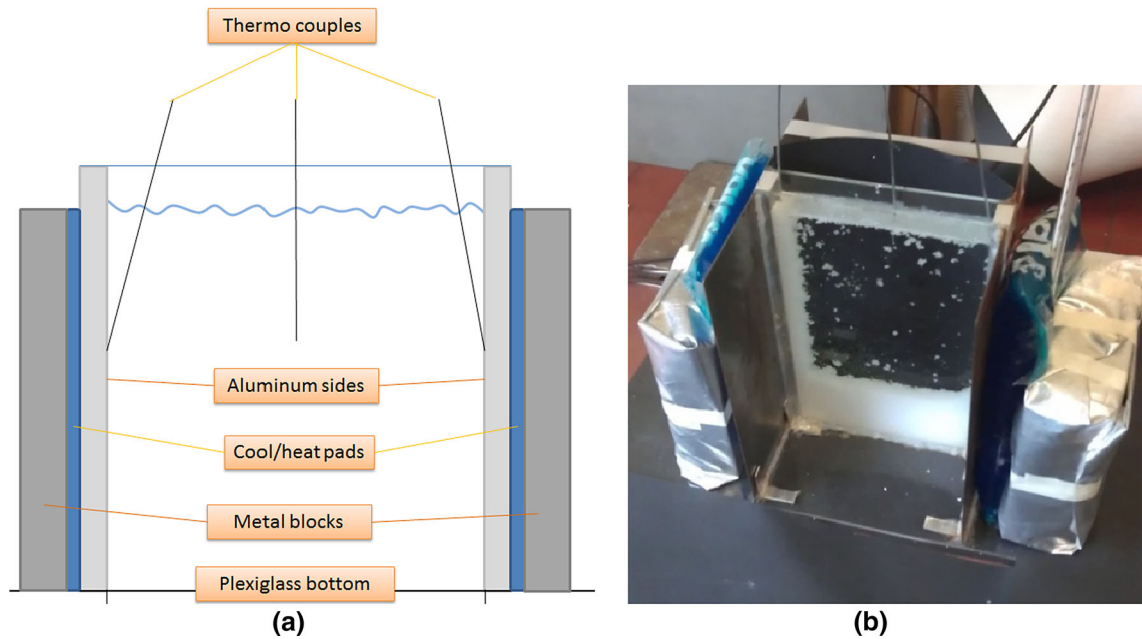


Fig. 3—(a) Schematic illustration of the water model and (b) square mold with thermocouples and cooling or heating pads integrated.

on one side, an adequate amount of solid crystals should be obtained for the experimental observation and, on the other side, experiments should be feasible to conduct. As the hot saturate solution was poured into the mold, crystallization started in the mold. The temperature of the solution was measured in the mold center and at the mold walls, and the “solidification” process was documented by high-resolution video camera and analyzed afterward.

IV. RESULTS AND DISCUSSION: HOT MODELING

A. Ingot Temperature Evolution

As discussed in Section II, the ingot temperature was measured during casting and solidification with two thermocouples. Figure 4 shows the measured temperature curves, which indicate that the solidus temperature was reached 142 minutes after pouring at a distance of 25 mm to the ingot centerline and 132 minutes at a distance of 100 mm. Since the last solidified region can be determined from the sulfur prints where the sulfur segregation is the most severe, it was found that the latest solidified spot, the so-called “hot spot,” appears at the ingot height of 370 and 24 mm away from the centerline, as illustrated in Figure 2. The thermocouple with the distance of 25 mm (thermocouple 1) to the ingot center is, thus, 49 mm away from the hot spot, and the other thermocouple (thermocouple 2) is 124 mm away. Based on the measurements, it can be deduced that the local solidification time at the hot spot is over 142 minutes and so is the total ingot solidification time. The reported total solidification time for a 3-t steel ingot in a square cast iron mold is 100 to 110 minutes^[26] and

for a 6 t hexahedron ingot in a cast iron mold is 260 minutes^[27]; therefore, it can be inferred that the total solidification time of the 500 kg slow-solidified ingot in the present study corresponds to the solidification time of industrial scale ingot with weight between 3 and 6 t.

From the first derivation of the temperature curve, the time points of liquidus and solidus temperature were found (shown in Figure 4). The time point for liquidus temperature $t(T_l)$ is determined, where the first derivation dT/dt curve turns from zero to negative and the time point for the solidus temperature $t(T_s)$ happens at the minimum of the dT/dt curve. The local solidification time θ_f can be calculated from Eq. [1].

$$\theta_f = t(T_s) - t(T_l) \quad [1]$$

The local solidification time was found to be approximately 35 minutes at the position of thermocouple 1, which is 25 mm from the ingot centerline and approximately 90 minutes at the position of thermocouple 2, which is 100 mm from the ingot centerline. The different local solidification time indicates an accelerated thermal/solutal cooling in the hot spot region when the final crater solidifies, and this will be discussed later, together with the as-cast microstructure.

B. A Segregates

The as-cast macrostructure of the ingot was revealed in sulfur prints in both longitudinal and transverse directions, as shown in Figures 5(a) and (b). The as-cast structure consists of columnar zone, columnar-to-equiaxed transition (CET) zone, the outer and inner equiaxed zones in the upper portion, and the sedimentation cone of the equiaxed grains in the lower portion of the ingot.

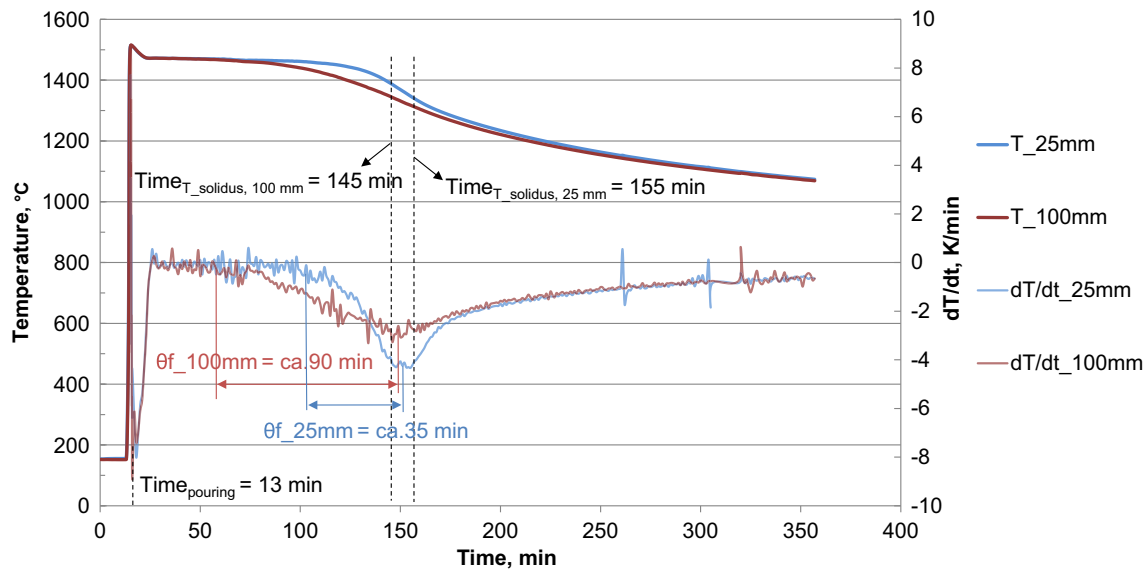


Fig. 4—Temperature curves recorded at 25 and 100 mm from the ingot center at the ingot height of 350 mm (corresponding to 150 and 75 mm from the side mold wall) and their derivations; θ_f is the local solidification time.

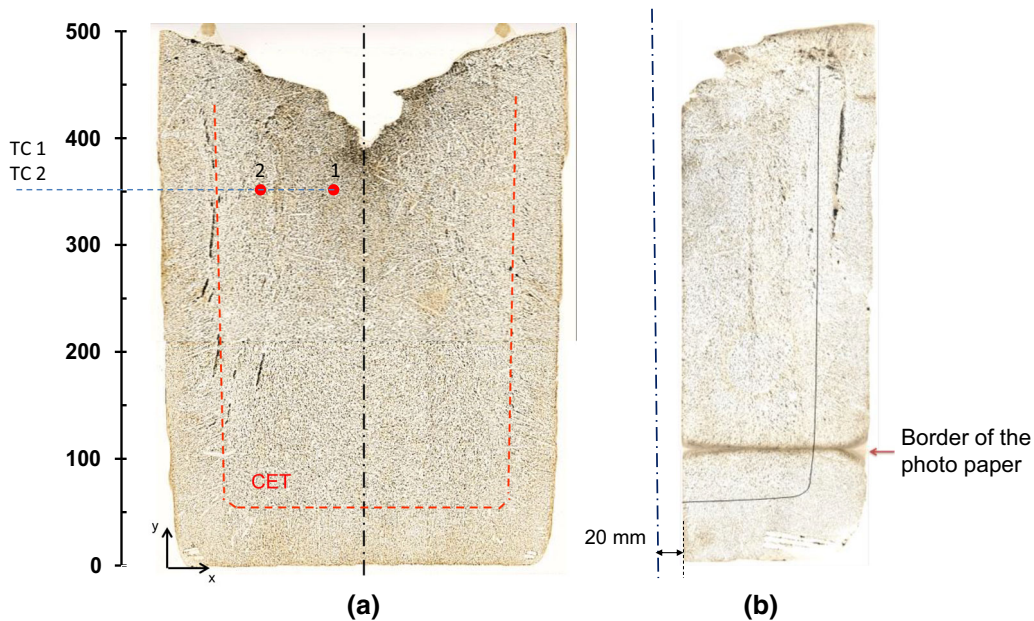


Fig. 5—Sulfur print of the longitudinal cross sections of the 500-kg ingot plane in (a), which is orthogonal to the plane in (b); ingot $H/D = 505 \text{ mm}/365 \text{ mm} = 1.38$.

The red dashed line in Figure 5 indicates the CET zone, which has a width of approximately 20 mm and covers the range between approximately 40 and 60 mm away from the ingot side surface. No V lines are found in the sulfur prints, and A lines appear at a distance of 40 to 100 mm from the ingot side surface at the ingot height of 120 to 470 mm. Based on the inclined angle of A lines, the A-segregation region can be divided into the outer and inner regions. In the outer region, which is 40 to 65 mm to the ingot side surface, A lines are inclined 5 to 10 deg to the center of the ingot, whereas in the inner region, which is 65 to 100 mm to the ingot

side surface, A lines are inclined 10 to 15 deg to the center of the ingot, especially in the lower portion of the ingot.

The outer A-segregation region overlaps partly with the CET zone, and the inner A-segregation zone lies mainly between the columnar zone and the sedimentation cone of equiaxed dendritic grains. Based on the fact that A segregates form in correlation with the structure development, the mechanism of A segregation at different locations of ingot might be different. Two types of A segregates and three mechanisms of A segregation are suggested in the present study.

The first type of A segregates appear at the outer A-segregation zone, which is mainly the CET zone among the columnar dendrite tips and equiaxed grains and also partly in the outer equiaxed zone, with the inclined angle of 5 to 10 deg to the center of the ingot. The segregated melt comes originally from the interdendritic fluid in the columnar zone. Since the segregated melt is enriched with light alloying elements, such as [C], [S], [P], and [Si], the melt is lighter compared to the bulk melt and tends to flow upward due to the solutal buoyancy force. In the CET zone, the grain structure is relatively loose in comparison to the columnar zone, and this benefits the interdendritic fluid to flow from the columnar zone through the CET zone and form small channels there. As solidification proceeds, channels develop upward and toward the center of the ingot until the inner equiaxed zone is reached and the grain structure becomes compact again. Furthermore, the enrichment of alloying elements reduces the liquidus temperature of the interdendritic melt, and dendrite arms could be dissolved during melt flowing by diffusion, which increases the instability of A-channel formation and the further widening and prolongation of A segregates.

The hot acid etched macrostructure indicates further that most of the A segregates occur at the location where dendrites are coarse and relatively loose compacted (Figure 6). The dark spots are the A segregates, which are more deeply etched in the transverse cross section. They appear mainly in the CET zone and the outer equiaxed zone. Through measurement of the secondary dendrite arm spacing (SDAS), it was found that the dendrites at the CET zone and the outer equiaxed zone are relatively coarser than those in other area, and this will be presented in Section IV-C.

The other type of A segregates occur at the inner and lower part of the ingot especially at the boundary of the sedimentation cone of the equiaxed grains, with an inclined angle of 10 to 15 deg to the center of the ingot. There are two mechanisms to describe the formation of this type of A segregates.

The first mechanism is that the segregated melt comes from the interdendritic fluid in the sedimentation cone of equiaxed grains. As the equiaxed grains settle down onto the sedimentation cone and accumulate there, the ferrostatic pressure in the sedimentation cone increases

and the interdendritic melt will be squeezed out of the sedimentation cone and flow upward along the boundary of the cone; A segregates are formed there.

The second mechanism is that the sedimentation cone of equiaxed grains will shrink as solidification proceeds, and the shrinkage of the sedimentation cone induces a vacuum in the gap at the boundary of the sedimentation cone. Segregated melt is sucked into the gap and forms A segregate there. However, it is not yet clear in the present study which mechanism dominates the formation of the second type of A segregates, and further studies are still demanded to describe the local A-segregation mechanisms.

The macrostructure of the transverse cross section of the ingot was also revealed by sulfur printing, as shown in Figure 7(a). The transverse cross sections of the A lines are observed to be several “dark spots” with a diameter of 1 to 2 mm, named “A dots,” which cover an area with a width of approximately 50 mm around the CET zone. The distribution of these A dots was quantified with regard to ingot height and the distance to the ingot center. As shown in Figure 7(b), at each height of the ingot, a square shaped area in sulfur prints (illustrated by the red rectangular) was chosen for measurements. This square was then separated in several strips with a width of 10 mm, as illustrated by the blue rectangular. In each strip, the number of A dots was measured, and the results show a discretized distribution of A dots in the transverse direction from the ingot center to the surface at different heights of the ingot, as given in Figure 8.

Figure 8(b) shows that a peak appears in each plate with a maximum A-dot number, and the location of the peak moves toward the ingot surface as the height increases (except for the case at the ingot height of 120 mm, which is in the sedimentation cone of equiaxed grains). At the ingot height of 220 mm, the peak appears at the radius of 130 mm, whereas at the height of 410 mm, most of the A dots are found at the radius of 160 mm. Furthermore, the contours of the distribution profiles are different at different heights. At the height of 220 mm, the distribution profile is axial symmetric and the A-segregation zone is at the radius of 90 to 160 mm. At the ingot height of 305 mm, more A dots are found in

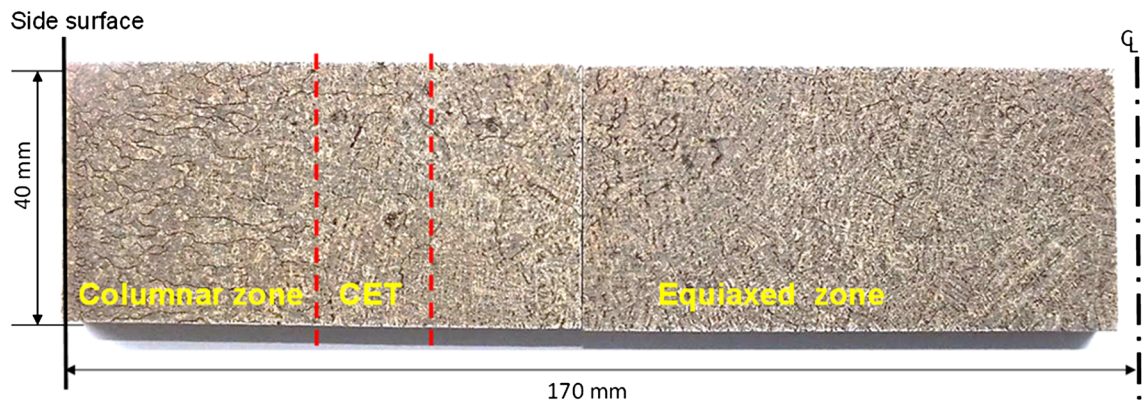


Fig. 6—Macro-etching of the transverse plate at the ingot height of 185 mm; A-segregates are more deeply etched as dark spots in the transverse cross section.

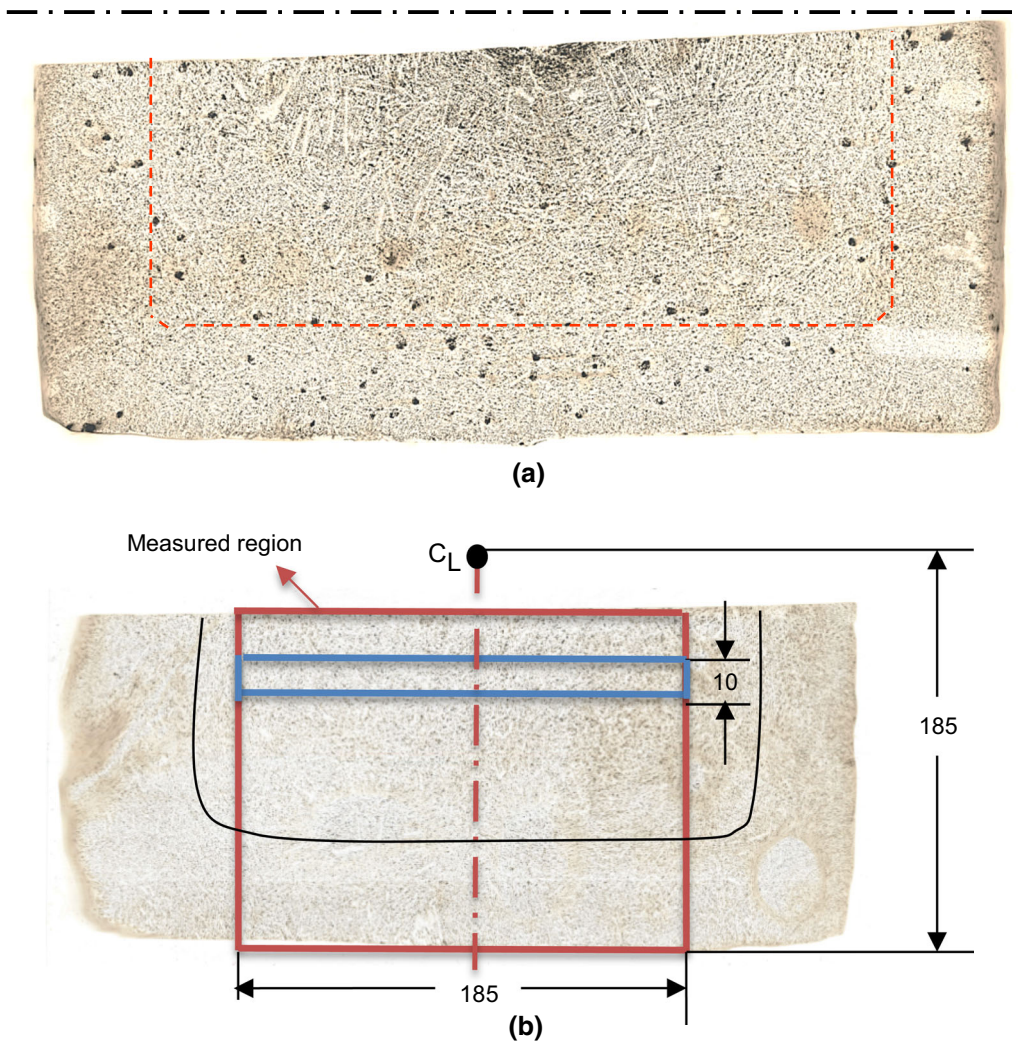


Fig. 7—(a) Sulfur print of the transverse plate, at the ingot height of 410 mm (red dashed line indicates the CET position), cross section $370 \times 165 \text{ mm}^2$, and (b) measuring area of A dots (solid black line indicates the CET position).

the inner part of the ingot and the A-segregation zone extends inward to the radius of 60 mm. At the ingot height of 410 mm, the A dots are not axial symmetric distributed where they appear at the radius of 160 mm and the A-segregation zone is extended inward to the radius of 40 mm.

Based on the quantitative measurements shown in Figure 8, the A-segregation zone in the 500 kg ingot is illustrated schematically with red color in Figure 9. The A-segregate zone covers a range with the radius from 40 to 170 mm at the ingot height from 120 to 470 mm. The shadow indicates the density of the A segregates in the A-segregation zone. In the upper portion of the ingot, A segregates appear mostly near the ingot side surface at the radius of 150 to 160 mm, and in the lower portion of the ingot, A segregates appear at the radius of 130 mm.

Compared to the macrostructure of industrial heavy ingots with the weight from 30 to 300 t,^[8,11] the 500-kg slow-solidified ingot shows similarity to the 30- and 65-t ingots in terms of the location of the A segregates; in both cases, A segregates appear in a narrow zone within the half radius of the ingot. In larger ingots with weight from

105 to 300 t, the A-segregation zone is much wider, covering a range of nearly the entire ingot width. Considering the mechanism of the first type of A segregation suggested in the present study, a long solidification time provides a broad time window for interdendritic fluid flow and remelting in channels, and thereby promotes the probability of formation and further development of A segregates in length and width.

Another similarity is that in industrial heavy ingots, A lines are relatively vertical in the upper part of the ingot and more inclined to the ingot center in the lower part of the ingot; this is consistent with the 500-kg ingot, in which the first type of A segregates in the outer and upper part of the ingot are inclined 5 to 10 deg to the center of the ingot and the second type of A segregates in the inner and lower part of the ingot are inclined 10 to 15 deg to the center of the ingot.

Two differences between the 500 kg and the industrial heavy ingots were also found. The first difference is that the A lines are longer and thicker in the heavy ingots, and this can be explained by the long solidification time in heavy ingots. The second difference is that V

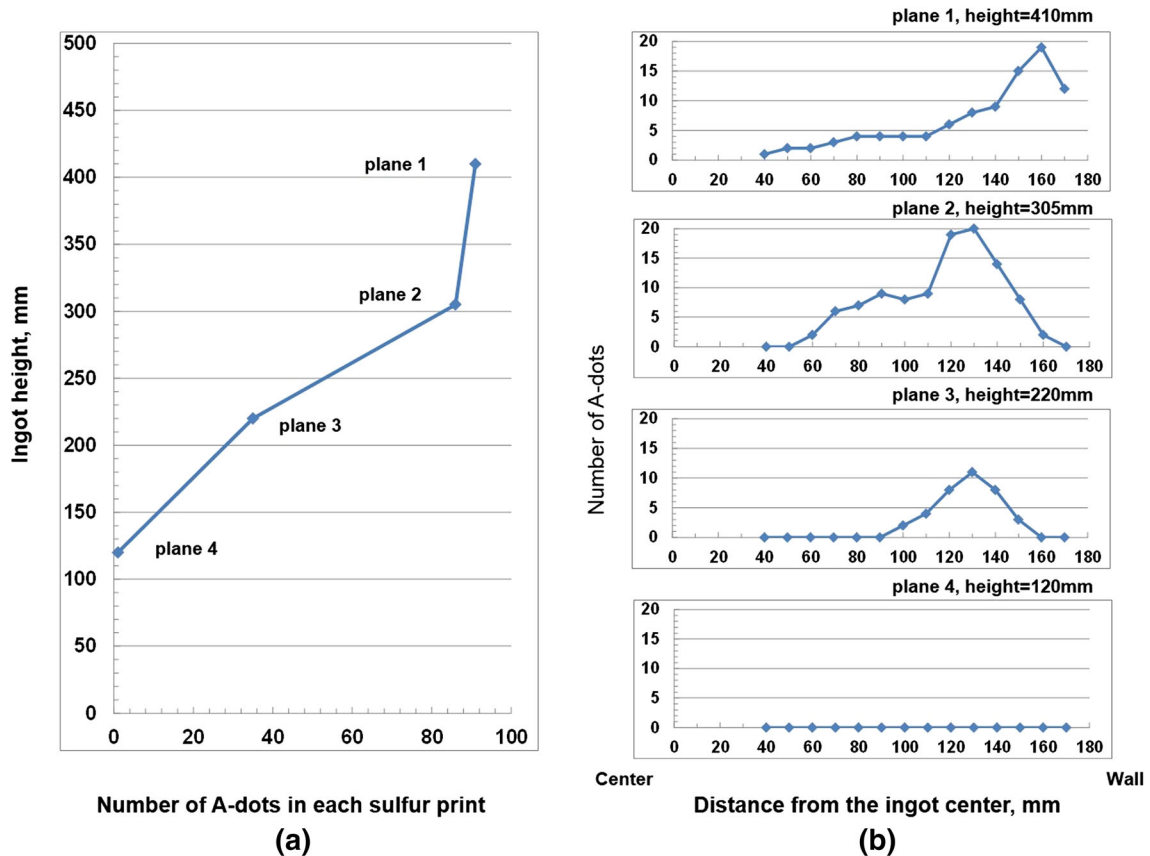


Fig. 8—Distribution of A dots in sulfur prints of the transverse plates: (a) total number of A dots at different ingot heights and (b) distribution of A dots in the transverse direction at different ingot heights.

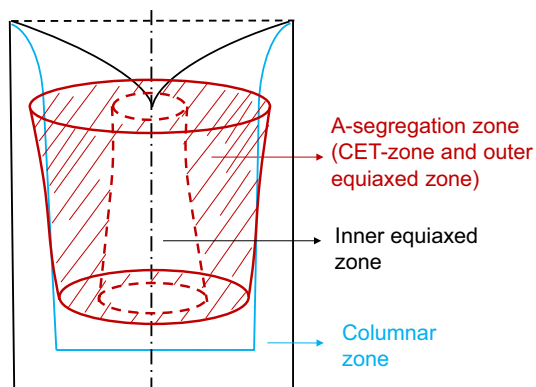


Fig. 9—Schematic illustration of the A-segregation zone in the as-cast 500-kg ingot.

segregates are not found in the 500-kg ingot, whereas in the 30-t^[8] and 65-t^[11] ingots, V segregates were observed in sulfur prints, and in the 105- and 300-t ingots,^[8] no clear V lines were found. The formation of V segregates could be explained in correlation with the ingot H/D ratio. The H/D ratio of the 500-kg ingot is 1.38, which is close to the 300 t ingot with H/D ratio of 1.39. In thick ingots with low H/D ratio, due to the ingot width, it is not possible to build dendrite bridges between two columnar solidification fronts in the ingot center, which is necessary for the formation of V segregates.

C. Secondary Dendrite Arm Spacings

The dendrite structure was further quantified by measuring the SDAS in the transverse direction of the ingot using light optical microscopy. For each sample, at least 10 values of the SDAS were measured and an averaged value was calculated. Figure 10 shows the measured SDAS values along the transverse direction at the ingot height of 410 mm, which is directly under the top cavity, and at the ingot height of 120 mm, which is in the sedimentation cone of equiaxed grains.

The measured SDAS can be correlated to the local solidification time by using the empirical Eqs. [2] and [3] suggested by Jacobi and Schwerdtfeger^[28]:

$$\lambda_2 = A \cdot \theta_f^B \quad [2]$$

$$\theta_f = \left(\frac{\lambda_2}{A} \right)^{\frac{1}{B}} \quad [3]$$

where λ_2 is the SDAS in micrometers; θ_f is the local solidification time in seconds; A and B are constants, $A = 15.8$ and $B = 0.44$; and the values of A and B were already verified for the same steel grade by the experimental measurement for the 100-kg ingots.^[29]

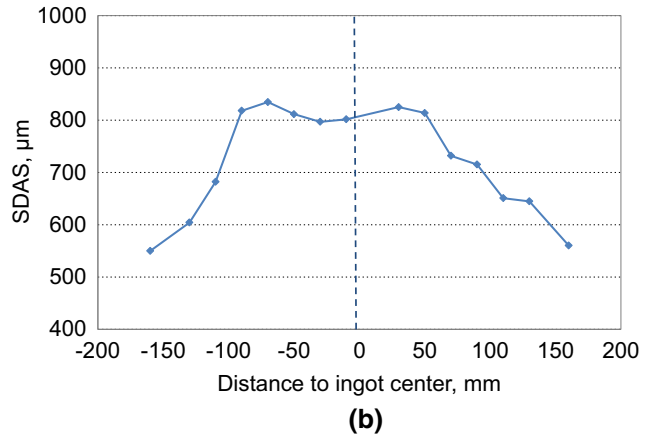
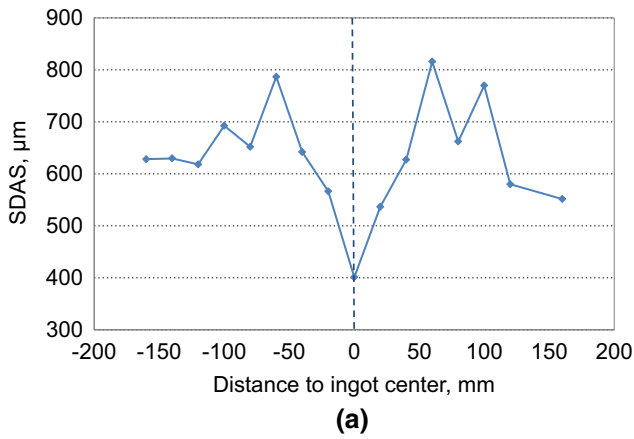


Fig. 10—Distribution of SDAS along the transverse direction: (a) at the ingot height of 370 mm (directly under the top cavity) and (b) at the ingot height of 120 mm (in the sedimentation cone).

The averaged SDAS values in the columnar zone were measured to be approximately 600 μm at different heights all over the ingot, which corresponds to a local solidification time of 65 minutes. In Figures 10(a) and (b), a higher SDAS value appears at the radius of 60 to 110 mm than that in the ingot center and in the columnar zone, and the maximum value is found at the radius of around 70 mm, which is approximately 800 μm at the ingot height of 370 mm and 820 μm at the ingot height of 120 mm. This corresponds to a local solidification time of around 125 minutes at the radius of 70 mm. The major difference between Figures 10(a) and (b) is in the ingot center: at the height of 370 mm, the dendritic structure is fine with the SDAS value of only 400 μm , corresponding to a local solidification time of 26 minutes, whereas in the sedimentation cone, the SDAS value is up to approximately 800 μm , corresponding to a long local solidification time of 125 minutes.

These results are consistent with the calculated local solidification time from the measured temperature curves in Figure 4. At the ingot height of 350 mm with a distance of 100 mm to the ingot center, the first derivations of the measured temperature curve indicate that the local solidification time is 90 minutes, and this corresponds to a calculated SDAS value of approximately 700 μm , which is consistent with the measured SDAS at the ingot height of 370 mm with a distance of 100 mm to the ingot center (Figure 10(a)). At the ingot height of 350 mm with a distance of 25 mm to the ingot center, the local solidification time is approximately 35 minutes from the temperature curve, which is quite close to the time (26 minutes) calculated from the SDAS value at the ingot height of 370 mm in the ingot center.

Generally, the SDAS value can be influenced by two factors: the driving force and the grain density. In the hot spot region, the driving force of dendritic growth is dominated by constitutional undercooling, as the last solidified melt is highly enriched with alloying elements. Under strong constitutional undercooling, the dendrites will grow fast; meanwhile, there is a large amount of equiaxed grains in the melt. Both factors lead to the low

SDAS value in the hot spot region. In the sedimentation cone of equiaxed dendrites, although there are adequate equiaxed grains, the SDAS value is the highest. In this area, thermal undercooling is not as strong as in the columnar zone, and the constitutional undercooling is also relatively small. Since the solute-enriched interdendritic melt is pressed out of the dendritic envelop by ferrostatic pressure, the solute concentration of the interfacial melt is lowered. Due to the low thermal and constitutional undercooling in the sedimentation cone, dendrites have enough time to grow and this leads to a high SDAS value there.

D. Macrosegregation

Macrosegregation of the alloying elements in the as-cast 500-kg ingots was investigated with regard to C, Mn, Si, Cr, S, P, and Al with the help of PDA-OES at IEHK, RWTH Aachen University.^[30,31] The PDA-OES method is a sparkle analysis method, which is used to specify the content of alloying elements and has the advantage of supplying reproducible quantitative results.^[31] The diameter of the measurement spot is around 5 mm, and at each spot, the content of alloying elements is measured and averaged. At least three measurements were conducted at each spot. As shown in Figure 11, samples were taken in the longitudinal direction of the ingot, which is approximately 20 mm from the ingot geometric centerline and also in the transverse direction at different ingot heights (120, 220, 370, and 410 mm).

The segregation index of alloying elements was calculated according to Eq. [4], where C_i stands for the measured content of the alloying element at the measuring spot and \bar{C}_i stands for the average composition of the alloying element over the ingot, which was determined by the averaged value of six measuring spots in the columnar zone at the middle height of the ingot.

$$\text{segregation index} = \frac{C_i - \bar{C}_i}{\bar{C}_i} \quad [4]$$

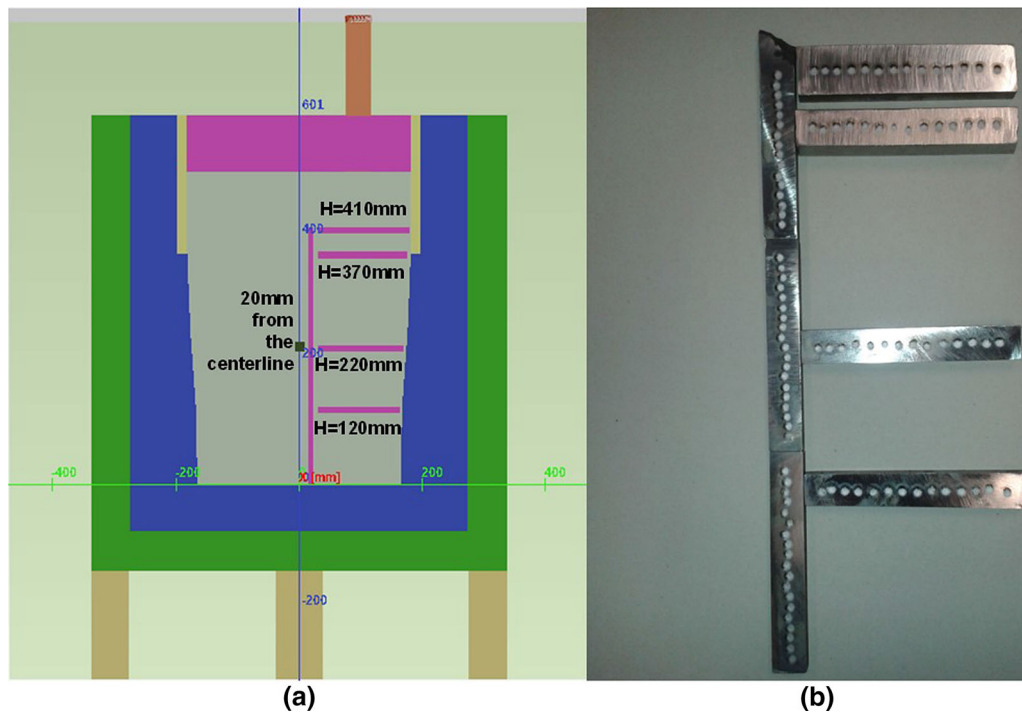


Fig. 11—Position of samples for the spectrometry analysis: (a) schematic illustration of the sample position and (b) samples after the spectrometry analysis.

Figure 12 shows the segregation index of carbon along the ingot longitudinal and transverse directions. In the lower portion of the ingot, negative segregation is found with the macrosegregation index of -0.05 . This indicates that the height of the sedimentation cone of the equiaxed dendritic grains is up to approximately 250 mm in the ingot center. In the transverse direction, the segregation index of carbon is negative within the radius of 120 to 130 mm at the ingot height of 120 to 220 mm, implying the contour of the sedimentation cone. As the half ingot width is 180 mm and the columnar zone has a width of 50 to 70 mm, the boundary of the sedimentation cone lies exactly at the columnar front in the lower part of the ingot with the height between 120 and 220 mm. In the upper portion of the ingot, positive segregation appears, mainly in the ingot center with radius up to 70 to 80 mm. Peaks of positive segregation are found at the radius of 100 to 140 mm at the CET zone and the outer equiaxed zone, which is due to the presence of A segregates.

The maximum positive segregation index of carbon is 0.38 at the ingot height of 370 mm, corresponding to the carbon concentration of 0.74 pct with the averaged concentration of 0.538. Considering the ingot total height of 500 mm as H_{\max} , the maximum carbon macrosegregation appears at the height where H/H_{\max} equals 0.74. Figure 13 summarizes the carbon macrosegregation along the centerline of large industrial scale ingots from 5 to 650 t in the previous study.^[3,12–17] The segregation index is calculated after Eq. [4]. The maximum carbon segregation index in the 5 t ingot is 0.5 at the height where H/H_{\max} equals 0.8 and in the 6.2 t ingot is 0.42 at the maximum ingot height. As the ingot weight increases, the maximum carbon segregation is

higher. The macrosegregation of carbon in the present study is comparable to the ingots with weights around 5 to 6.2 t, and this is also consistent with the fact that the total solidification time of the 500 kg ingot corresponds to the ingot with weight between 3 and 6 t, as discussed in Section IV–A.

Other alloying elements, such as manganese, silicon, sulfur and phosphorous, show the similar tendency that positive segregation occurs in the upper portion and negative segregation appears in the lower portion of the ingot. Figure 14 shows the segregation index of sulfur and phosphorous along the ingot centerline and in the transverse direction at different heights. Compared to the carbon macrosegregation shown in Figure 12, the macrosegregation curves of sulfur and phosphorous are more scattered. This can be explained by the fact that sulfides and phosphides are distributed all over the ingot and the appearance of sulfides and phosphides at the PDA-OES measuring spot will influence the averaged content of sulfur and phosphorous of the measurement.

Along the ingot centerline, the maximum segregation index of sulfur is 1.5 at the ingot height of 370 mm, whereas the maximum segregation index of phosphorous is 0.9 at the same height. In the transverse direction of the ingot, the maximum segregation index of around 3 is found at the radius of approximately 130 mm for both sulfur and phosphorous. At the other height of the ingots, peaks are also found, and this can be explained by the appearance of A segregates at the measuring spot.

Contrary to other alloying elements, aluminum shows a different segregation behavior, as shown in Figure 15. In the sedimentation cone of the equiaxed dendrites, aluminum is not segregated. A few peaks of the

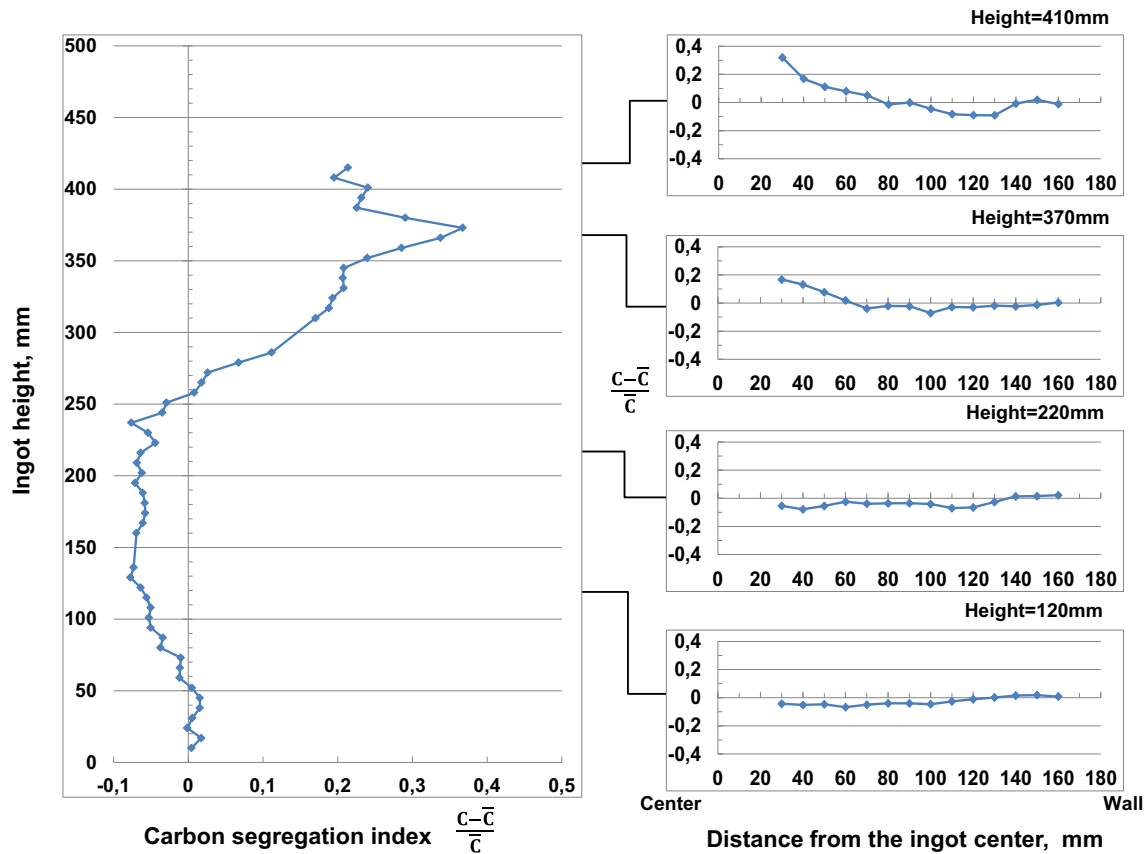


Fig. 12—Segregation index of carbon along the ingot centerline and in the transverse direction at different heights.

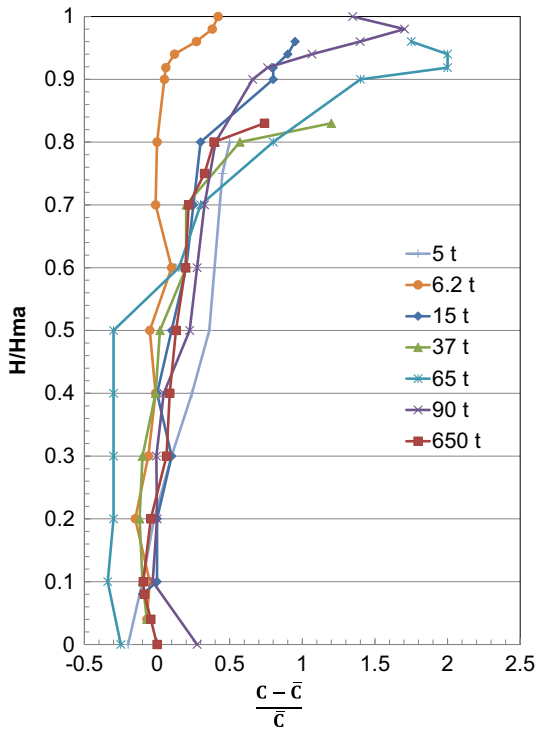
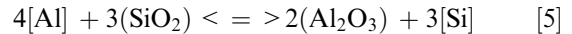


Fig. 13—Segregation index of carbon along the centerlines of 5-, 6.2-, 15-, 37-, 65-, 90-, and 650-t steel ingots.^[3,12-17]

segregation index appear, which can be explained by the finding that single or an agglomeration of aluminum oxides were caught by equiaxed dendrites during sinking and brought into the sedimentation zone, and these aluminum oxides were detected by spectrometry measurements.

In the hot spot region, aluminum is strongly negatively segregated, and this can be explained as follows: on one hand, iron content is lower in the upper portion of the ingot as the other alloying elements are enriched, and the dissolved aluminum content in iron is also lowered; on the other hand, the dissolved aluminum can react with SiO_2 from the anticavity powder and form Al_2O_3 particles, which could float up and form slag,^[32] as given in Eq. [5]. Through this reaction, the dissolved aluminum near the top of the ingot is consumed and repelled out of the ingot, and this leads to lower aluminum content in the upper portion of the ingot.



E. Mesosegregation

The segregation of alloying elements at A segregates was investigated using EPMA. Figure 16 shows the concentration map of four alloying elements, [C], [Si], [Mn] and [S], in the longitudinal cross section of an A segregate and its surroundings. The lightness corresponds

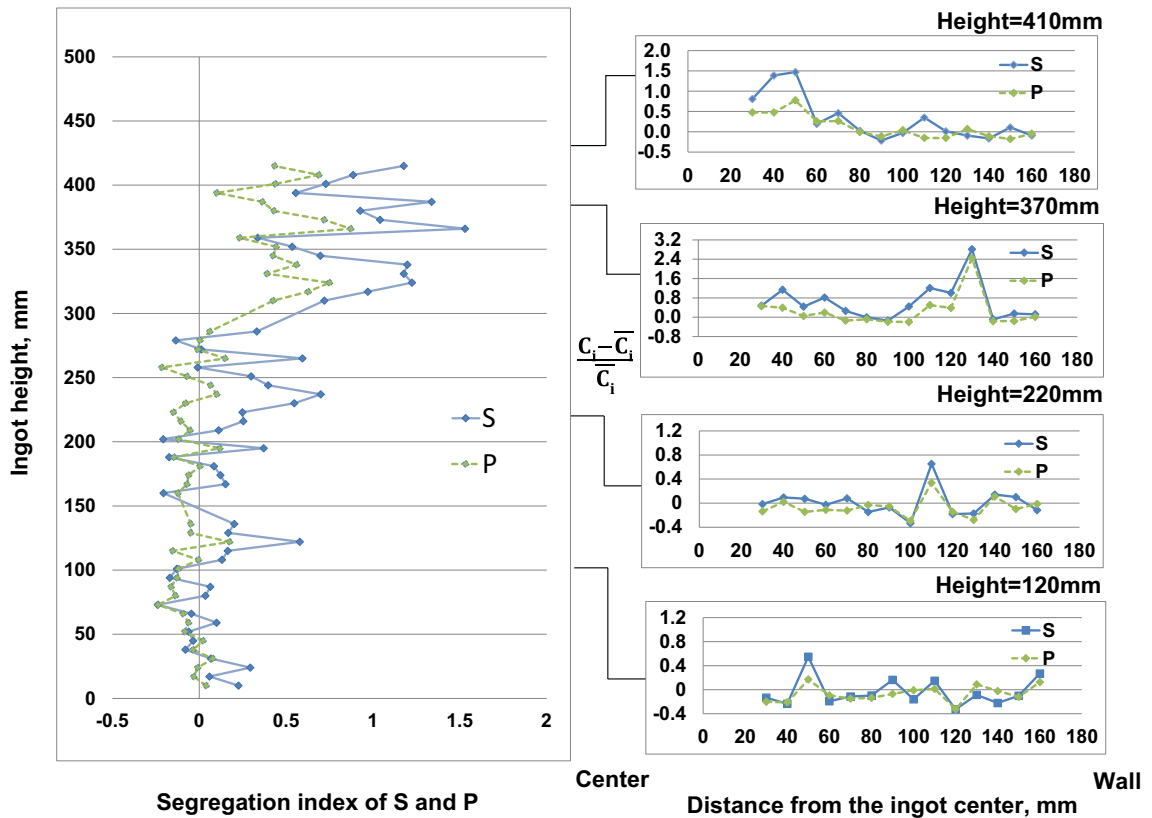


Fig. 14—Segregation index of sulfur and phosphorous along the ingot centerline and in the transverse direction at different heights.

to the intensities of characteristic X-rays of the alloying element, and higher lightness indicates higher concentration. In Figures 16(a), (c), and (d), a lighter region with the width of around 2000 μm , slightly inclined, can be observed, and this region is the A segregate. At the A segregate, the element concentration is higher compared to its surroundings. For sulfur, there is no apparent lighter region observed in Figure 16(b); instead, numerous light spots are found at the A-segregate region, indicating a large amount of sulfides there. Comparison of Figures 16(b) and (c) shows that the light spots in both [S] and [Mn] concentration maps overlap with each other, indicating that MnS particles formed due to highly segregated manganese and sulfur at A segregates. For silicon, light spots are also found in the concentration map at other locations, indicating that another kind of inclusion particle appears at the A segregate.

The measured maximum contents of the four alloying elements at the A segregate through EPMA are given in Table II. The measured [C] content at the A segregate is up to 1.06 wt pct (without carbides), whereas the average carbon concentration of the entire ingot measured with PDA-OES in the columnar zone is 0.538 wt pct. The carbon segregation index at the A segregate is up to 0.97, which is much higher than the segregation index measured by PDA-OES in Figure 13, as the appearance of carbides at the A segregate increases the averaged value. Similarly, the other three elements are also found to be highly segregated at the A segregate with a high value of the segregation index, especially sulfur. The measured segregation values at the A

segregates provide experimental data for the validation of numerical simulation models of local remelting and channel formation during ingot solidification.

V. RESULTS AND DISCUSSION: COLD MODELING

The cold modeling experiments simulate the ingot crystallization process near room temperature. As the saturated NH_4Cl aqueous solution is poured into the cold square mold, solidification starts. Columnar dendrites grow from the side surfaces toward the mold center, and crystals precipitate near the cold side surface. Due to cooling conditions at the mold side surfaces, natural convection takes place and brings free crystals to the center of the mold. Large crystals sink and form the sedimentation layer of equiaxed dendrites, and small crystals are taken by the central ascending flow and move upward. Figure 17 gives an example of solidification at different stages in the cold mold.

A. Columnar Dendritic Growth

The width of the columnar zone at the middle height of the mold was measured at different time points after pouring, and the growth rate of the columnar dendrites was calculated. The measured values were then fitted to the square root law, which is usually used in continuous casting processes, as given in Eq. [6].

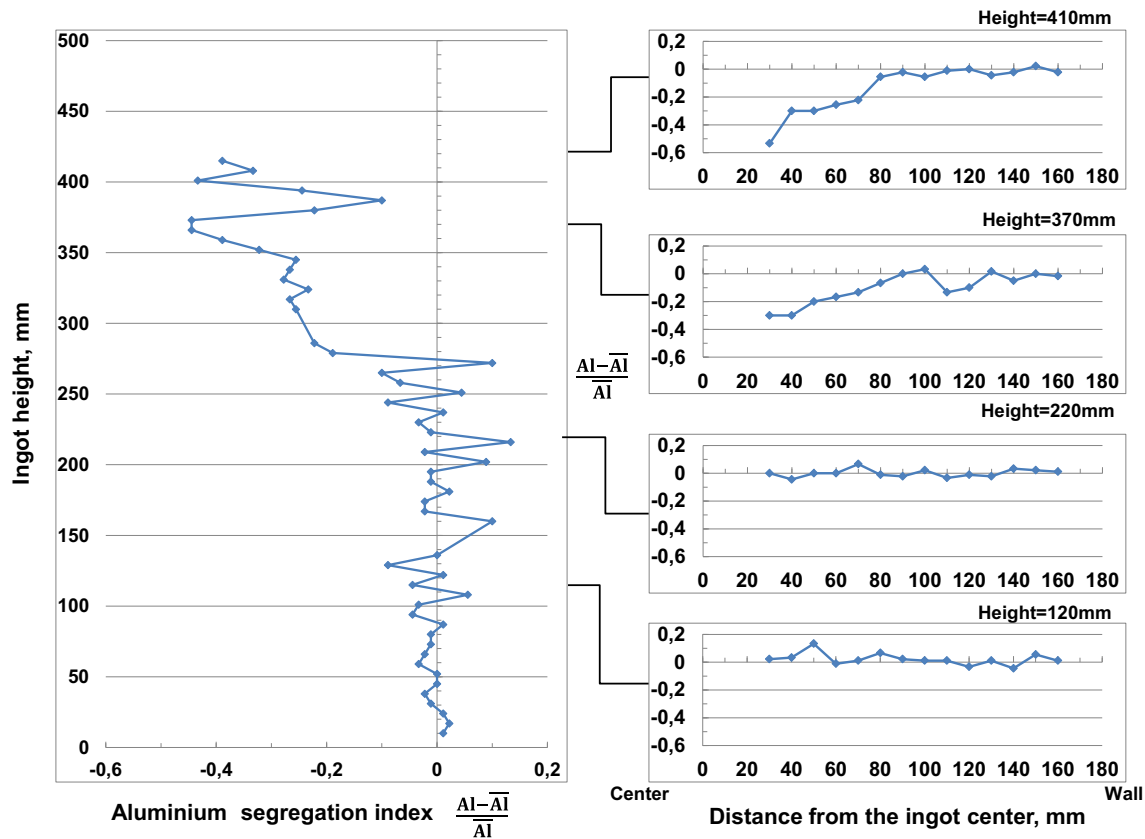


Fig. 15—Segregation index of aluminum along the ingot centerline and in the transverse direction at different heights.

$$D = k\sqrt{t} \quad [6]$$

where D is the width of the solidification shell in millimeters, t is the solidification time in minutes, and k is the solidification constant. Here, in the present study, k is used to describe the growth rate of the columnar dendrites.

Figure 18 shows the profiles of the measured width of the columnar e zone for the case with both sides cooling. The solidification constant k was calculated to be $4.49 \text{ mm}/\text{min}^{0.5}$ at the left side and $4.23 \text{ mm}/\text{min}^{0.5}$ at the right side. In the continuous casting process, the value of the solidification constant is usually over $20 \text{ mm}/\text{min}^{0.5}$.

There are certain factors that lead to the different k values in continuous casting and cold modeling. One important factor is the different cooling intensities; besides that, liquid flow could break the weak NH_4Cl -dendrite arms and reduce the columnar zone width, bringing more free crystals to form the inner equiaxed zone. Nevertheless, despite these differences, cold modeling provides the chance to observe complex macroscopic solidification phenomena in heavy ingots directly, such as sedimentation of free crystals, fluid flow, and channel formation.

B. Sedimentation of Equiaxed Grains

During solidification in the cold model, small equiaxed grains are carried upward by the central ascending flow, and as they grow, they will sink due to the density difference between the liquid and solid phases and form the sedimentation layer of equiaxed grains. These grains can grow while sinking, and large grains sink faster than the smaller ones because they are denser. In order to investigate the sinking phenomenon, a few sinking grains were traced by high speed video camera; the positions of these grains were recorded at different time points, and the sinking velocities of the individual equiaxed grains were then calculated. Figure 19(a) illustrates the measurement schematically, and Figure 19(b) shows the position profiles of seven grains at different time points after pouring. As most of the grains are formed in the vicinity of the water level due to the low temperature there, the initial position is considered to be at the water level. The distance between the individual grain and the water level (defined as NN) was measured at different time points while sinking.

The results show that the sinking velocity increases while sinking, and this is consistent with the results reported by Appolaire *et al.*^[33] In the early stage of solidification, equiaxed grains are small and sink slowly.

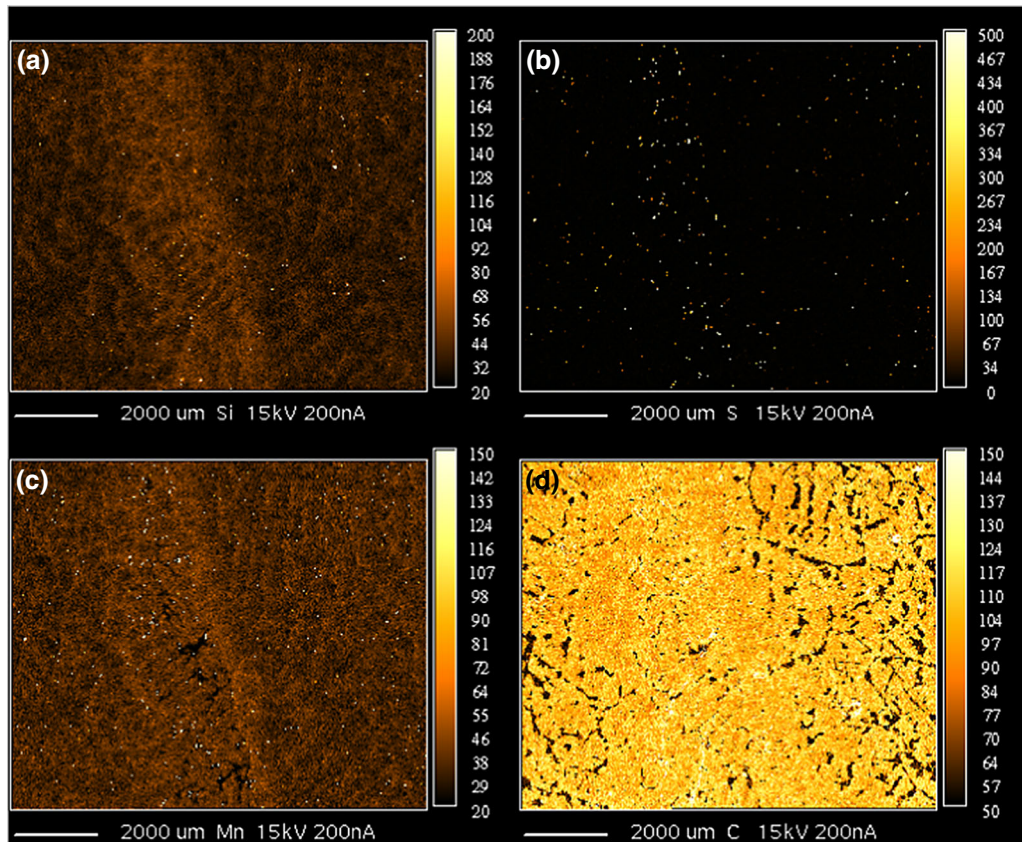


Fig. 16—Electron-based scatter intensity map of EPMA measurements, in the longitudinal cross section of an A segregate in the as-cast 500-kg ingot: (a) [Si], (b) [S], (c) [Mn], and (d) [C].

Table II. Maximum Content of Alloying Elements as well as Segregation Index at A Segregate, Measured by EPMA

Alloying Element	C	Si	Mn	S
Average content, \bar{C} , pct	0.538	0.378	0.538	0.0147
Maximum content, C_m , pct	1.06	0.629	0.718	0.032
Segregation index $(C_m - \bar{C})/\bar{C}$	0.97	0.67	0.34	1.17

Due to the thermal undercooling of the melt and the constitutional undercooling in the dendrite envelop, these grains grow further and become denser, and this accelerates sinking further; the sinking velocity can be increased to 5 mm/s. At the late stage of solidification (30 to 40 minutes after pouring), grains sink relatively slowly, with the sinking velocity up to 2 to 3 mm/s. Since the height of the sedimentation layer increases with time, there is limited space for the equiaxed grains to speed up in the late stage of solidification and the curves, therefore, are shorter. Meanwhile, due to the influence of the local turbulence above the sedimentation layer, the sinking velocity is also reduced in the late stage of solidification.

C. Two-Dimensional Fluid Flow

As one of the most complex macroscopic solidification phenomena, fluid flow plays an important role in the quality of final as-cast semiproducts, especially for those with large cross section. Conventional methods

offer a rare opportunity to gain insight into the solidification ingots, especially for heavy atom alloys, such as steel, and for large castings. By water modeling, the fluid flow pattern can be represented by the motion of the small particles and easily observed and analyzed. Two types of cooling conditions were studied in the present study, with regard to both sides cooling and one side cooling with the other side heating. The observed flow patterns are illustrated schematically with their major characteristics in Figure 20.

For the case of cooling at both sides, the flow pattern is axial symmetric and shows a classic natural convection pattern descending at the sides and ascending in the center (Figure 20(a)). Subjected to liquid drag force, the motion of the small equiaxed grains shares a similar pattern as the fluid flow, whereas large grains fall, especially near the cold walls. In front of the columnar dendrites, a local turbulence pattern was observed, as shown in Figure 20(b)). Local clockwise spiral turbulences start upward from the columnar front with the angle of 20 to 40 deg to the center of the mold, bringing

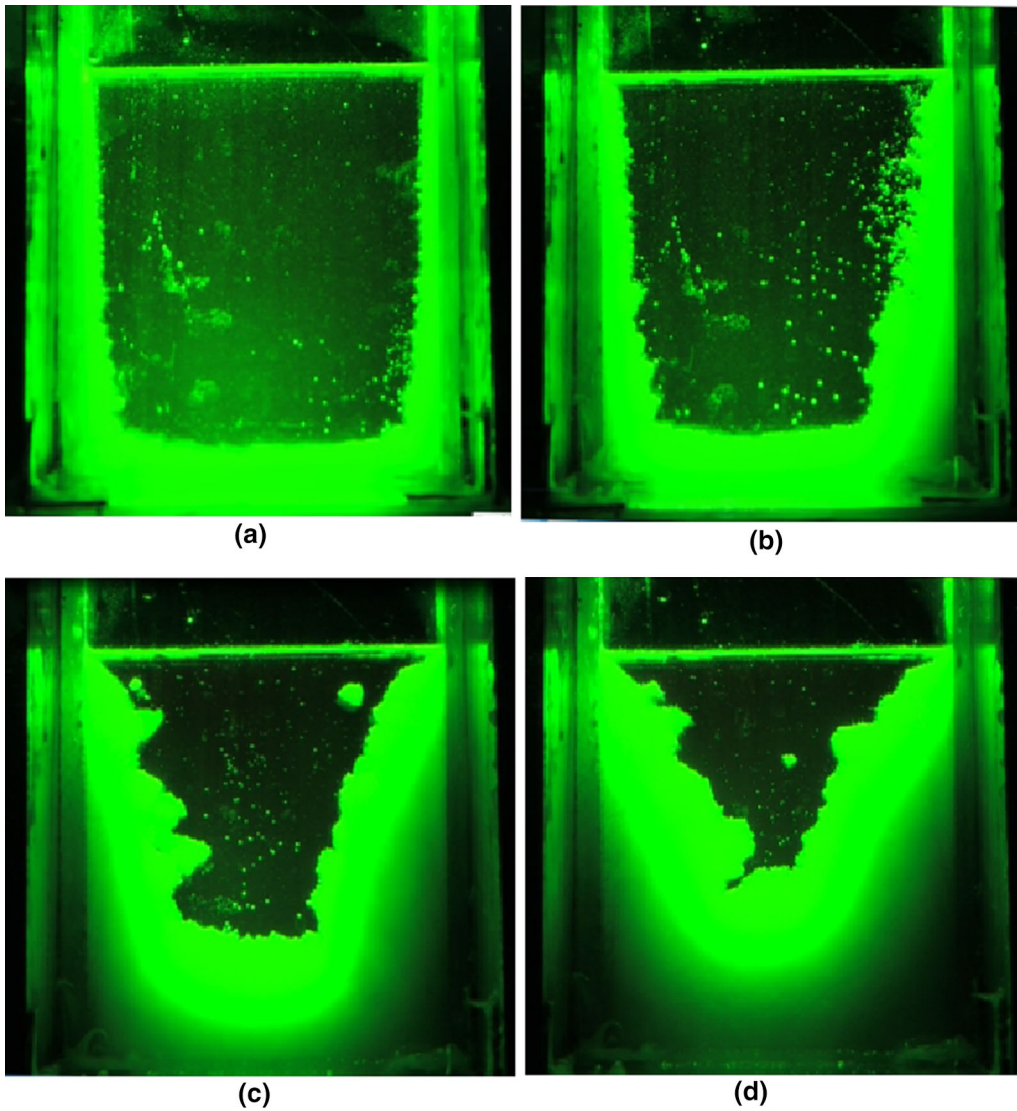


Fig. 17—Solidification at different time points after pouring (laser illuminated): (a) 10 min, (b) 15 min, (c) 25 min, and (d) 40 min.

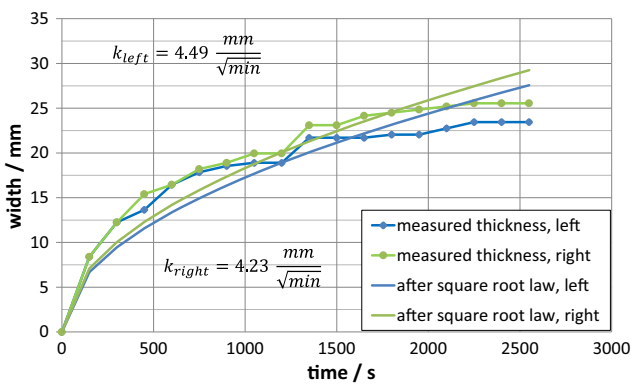


Fig. 18—Width of the columnar dendrite zone; both sides cooling.

the grains upward at first; then, these local turbulences join the main descending stream in front of the solidification front and bring equiaxed grains back to the bottom.

For the case with one side cooling and the other side heating, the flow pattern seems to be half of the case with both sides cooling. At early stages, the fluid flow obeys the classic natural convection pattern with the main stream flowing downward near the cool wall and upward near the hot wall, as shown in Figure 20(c). After a while, a narrow clockwise flow cycle is generated near the hot wall, as shown in Figure 20(d). Meanwhile, the main downward stream near the cold surface develops further into complex local turbulence in front of the columnar dendrite. Since the local spiral turbulence near the solidification front occurs only in the middle and later stages of solidification (Figures 20(b) and (d)), it is suspected that the formation of this local turbulence is related to the columnar dendritic structure. In the beginning of solidification, the cold surface is plain and smooth; however, after a certain period of time, the solidification front is composed of numerous dendrite tips, which appear periodically, and this could lead to local spiral turbulence.

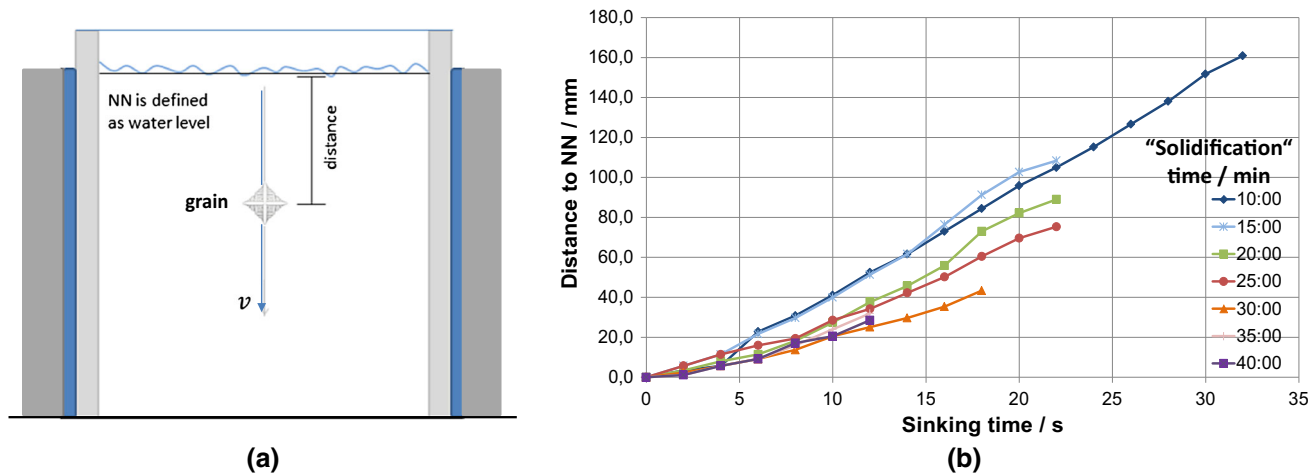


Fig. 19—(a) Measurement of distance between NN and the sinking grain and (b) distance to NN of grains vs sinking time, for seven different grains at different solidification time points after pouring.

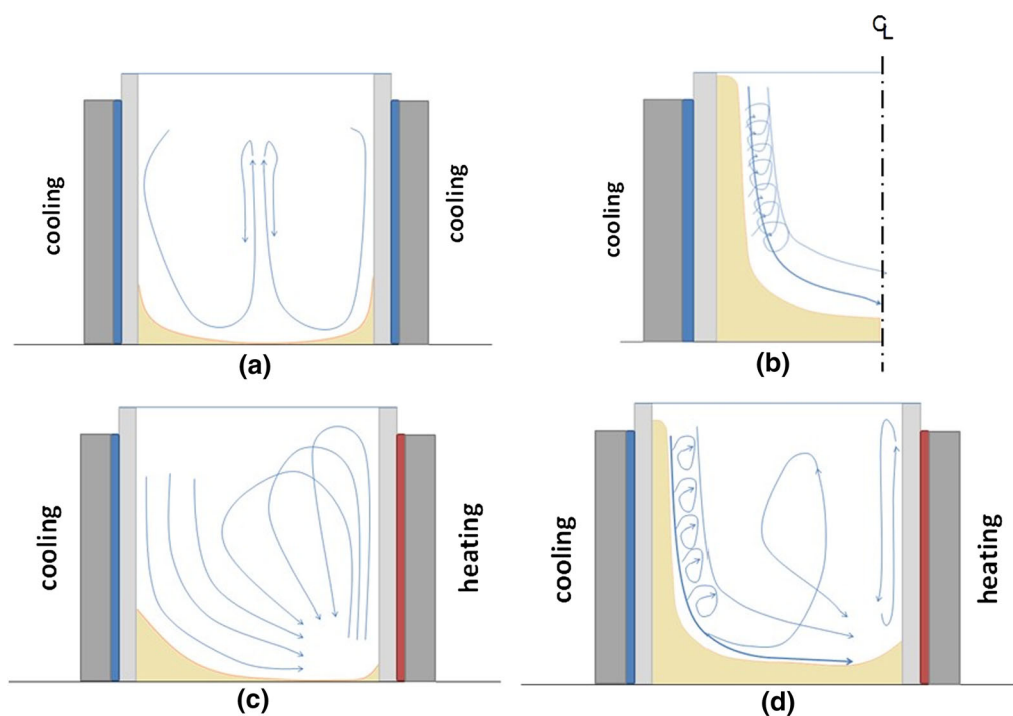


Fig. 20—(a) Schematic illustration of turbulence for both sides cooling, (b) local turbulences near the solidification front for both sides cooling, (c) schematic illustration of turbulence for one side cooling and one side heating in early stages of solidification, and (d) local turbulences near the solidification front for one side cooling and one side heating.

D. Channel Formation

Similar to the A segregates in as-cast ingots, cold modeling channels were also observed in cold modeling. Based on the different locations of these channels, two types of channels can be distinguished.

The first type of channels locate at the CET zone between the columnar dendrite tips and the sedimentation layer of equiaxed dendrites. Figure 21 shows the channel evolution with cooling at the left side and heating at the right side. As soon as the settled equiaxed crystals block the columnar dendrite tips mechanically,

the channel initiates. In this transition area, dendrites are loosely compacted, and no grains can sink to this area to close the channel. As solidification proceeds, the channel develops along with the sedimentation bed and, finally, forms a long and wide channel in the CET zone.

The second type of channels are much thinner in comparison with the first type. They appear also in the columnar zone, which is closer to the mold wall, as shown in Figure 22, with both sides cooling. The initiation of the second type of channel is difficult to distinguish, and as solidification proceeds, these

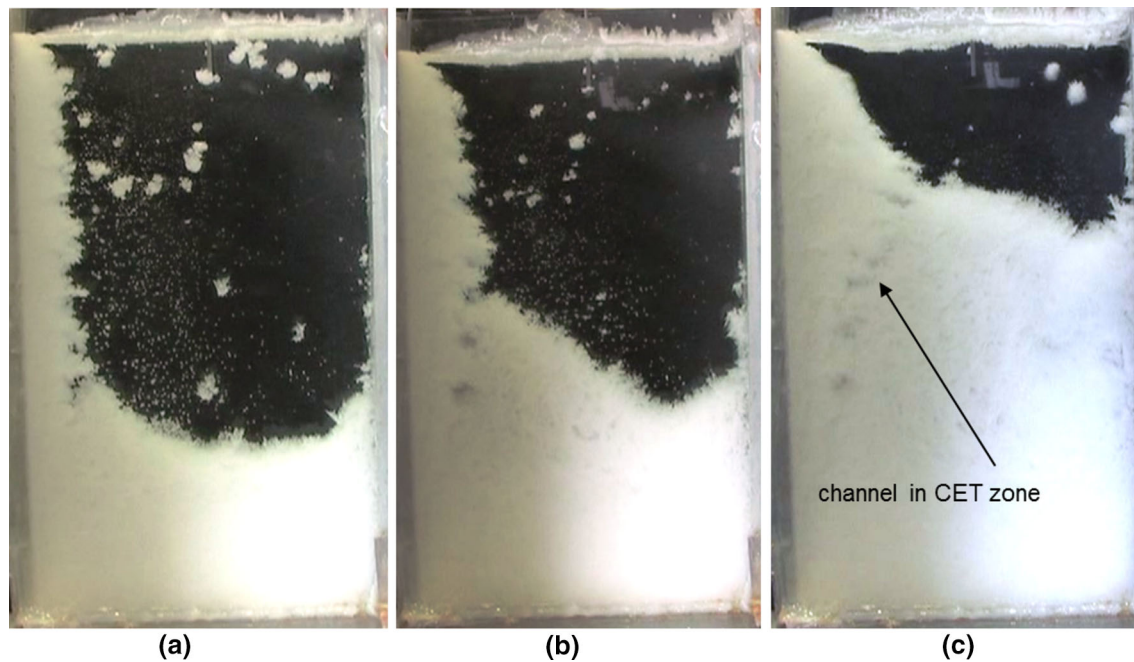


Fig. 21—Evolution of the first type of channels in the water model: (a) in the early stage of solidification, (b) in the middle stage of solidification, and (c) in the late stage of solidification.

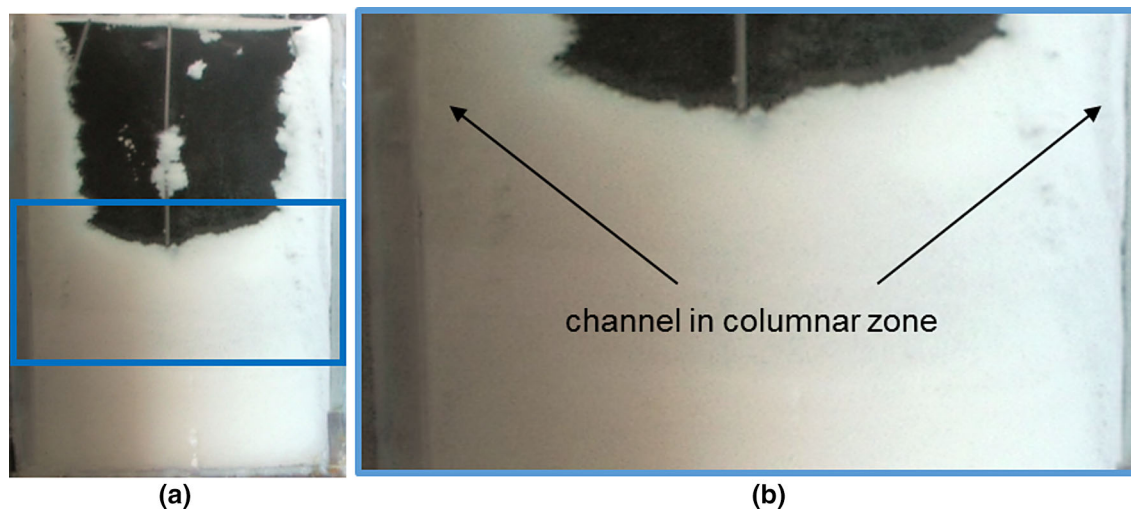


Fig. 22—Second type of channels in the water model: (a) channels in the late stage of solidification and (b) close view of channels in the columnar zone.

channels become more apparent. Different from the first type of channels in which only a single thick channel is found in the CET zone, several of the second type of channels appear in the same columnar zone. Based on the appearance time and location of the channels, it is speculated that the second type of channels are formed in correlation with remelting in the columnar zone.

It should be noted that certain differences exist between cold modeling and ingot solidification; however, as a result of the similarity between NH_4Cl crystallization and metal solidification in terms of dendritic growth, fluid flow and sedimentation of free crystals, as well as channel formation, complex

macroscopic phenomena in heavy ingots and continuous cast products can be modeled and observed using the salt-water system.

The hot and cold modeling are both methods to simulate the solidification process of large ingots. Similar phenomena were observed in both hot modeling and cold modeling; for example, the locations of the two types of A segregates are similar to the two types of channels in cold modeling, where the first type of channels are in the CET zone and the second type of channels are in the columnar zone. This could provide information for the validation of the A-segregation mechanisms. By analysis of channel formation regarding

channel initiation, channel growth/reduction, and the channel existing time, the phenomena of channel formation can be investigated from another aspect. In addition to that, other solidification phenomena observed in the cold modeling provide new insight for the investigation of ingot solidification, such as the interaction of fluid flow with free crystals, with columnar dendrites at the solidification front, and with sinking free crystals.

Furthermore, by integration of modern technology, such as particle image velocimetry and laser-induced fluorescence,^[34,35] into cold modeling, the temperature and concentration field can be quantitatively investigated and used as data for the validation of mathematical and numerical models.

VI. CONCLUSIONS

1. The total solidification time of the 500 kg insulated ingots is over 140 minutes, corresponding to the solidification time of ingots with weight between 3 and 6 t.
2. Two types of A segregates were observed in sulfur prints of the as-cast 500 kg ingots, and three mechanisms of A segregation were suggested. The first type of A segregates initiate in the columnar zone and are widened and prolonged through remelting by the solute-enriched interdendritic melt, and the second type locate between the sedimentation cone and the columnar zone and develop together with the sedimentation cone. In one mechanism, the solute-enriched interdendritic melt is pressed out of the sedimentation cone due to ferrostatic pressure, gathers at the boundary of the sedimentation cone, and forms A segregates. In the other mechanism, the segregated melt is sucked into the gap between the sedimentation cone and the columnar zone due to solidification shrinkage of the sedimentation cone and forms A segregates there.
3. SDAS was measured to be the lowest (400 μm) at the hot spot area and the highest (800 μm) in the middle of the sedimentation cone, which corresponds to the short local solidification time of 26 minutes at the hot spot area and the long local solidification time of 125 minutes in the sedimentation cone. This indicates fast grain growth at the hot spot area when the final crater solidifies. The maximum carbon macrosegregation index $\frac{C-C}{C}$ was measured to be 0.38, corresponding to carbon macrosegregation in ingots with the weight of 5 to 6.2 t.
4. Local spiral turbulences in front of columnar dendrite tips were observed in the middle and late stages of solidification in cold modeling trails.
5. Two types of channels were observed in the cold modeling trials, with the first type appearing between columnar dendrite tips and the sedimentation bed of free crystals and the second type appearing in the columnar zone near the cold mold wall. The locations of the two types of channels in cold models are similar to the locations of the two types of A segregates observed in the 500-kg ingots.

ACKNOWLEDGMENTS

The authors appreciate the technical assistance provided by M.Sc. Fangwei Zhai and M.Sc. Yijiang Xu during the experiments and are thankful to the Aktiengesellschaft der Dillinger Hütte for cutting the raw ingots. Many thanks are also extended to RHI Aktiengesellschaft and Lech-Stahlwerke for sponsoring the refractory and experimental raw metal materials.

REFERENCES

1. *Annual Report*, China National Erzhong Group, Deyang, China, 2012, p. 17.
2. <http://www.cfhi.com/yzjt/contents/273/2340.html>. Accessed 25 June 2009.
3. K. Kajikawa, S. Suzuki, F. Takahashi, S. Yamamoto, T. Suzuki, S. Ueda, T. Shibata, and H. Yoshida: Development of 650-Ton-Class Ingot for Turbine Rotor Shaft Forging Application, *ICRF 2012*, Aachen, Germany, 2012.
4. D. Senk: *Proceedings of the 6th International Congress on the Science and Technology of Steelmaking (ICS)*, Beijing, 2015, pp. 19–26.
5. *CITIC Pacific Annual Report*, Xingcheng Special Steel, Jiangyin, 2010, p. 18.
6. D. Senk, R. Wolff, Z. Chen, and P.V. Schweinichen: Solidification Research—Key to Best Products and Processes. *METEC 2011*, Düsseldorf, Germany, 2011.
7. J. Eisenkolb, R. Fandrich, and H. Jung: *Stahl Eisen.*, 2010, vol. 130, pp. 28–44.
8. J. Delorme and M. Laubin: *Casting Solidif. Steel*, 1977, vol. 1, pp. 214–76.
9. J.R. Blank and F.B. Pickering: *The Solidification of Metals*, Iron and Steel Institute, London, 1968, pp. 370–76.
10. M.C. Flemings and G.E. Nereo: *Trans. TMS-AIME*, 1967, vol. 239, pp. 1449–61.
11. G. Lesoult: *Mater. Sci. Eng. A*, 2005, vols. 413–414, pp. 19–29.
12. J.P. Gu and C. Beckermann: *Metall. Mater. Trans. A*, 1999, vol. 30A, pp. 1357–67.
13. P. Machovčák, A. Opler, Z. Carbol, A. Trefil, K. Merta, J. Zaoral, M. Tkadlečková, and K. Michalek: *Arch. Mater. Sci. Eng.*, 2012, vol. 58, pp. 22–27.
14. D.R. Liu, X.H. Kang, B.G. Sang, and D.Z. Li: *Acta Metall. Sinica*, 2011, vol. 24, pp. 54–64.
15. A. Kumar, M. Založnik, and H. Combeau: Experimental and Numerical Studies on the Influence of Hot Top Conditions on Macrosegregation in an Industrial Steel Ingot, *ICRF 2012*, Aachen, Germany, 2012.
16. L. Hartmann, C. Ernst, and J.S. Klung: Simulation of Ingot Casting Processes at Deutsche Edelstahlwerke GmbH, Witten, *ICRF 2012*, Aachen, Germany, 2012.
17. H. Combeau, A. Kumar, M. Založnik, I. Poitraul, G. Lacagne, A. Gingell, T. Mazet, and G. Lesoult: Macrosegregation Prediction in a 65 Ton Steel Ingot, *ICRF 2012*, Aachen, Germany, 2012.
18. I. Ohnaka: *Trans. Iron Steel Inst. Jpn.*, 1986, vol. 26, pp. 1045–51.
19. E.J. Pickering: *ISIJ Int.*, 2013, vol. 653, pp. 935–49.
20. C.Y. Wang and C. Beckermann: *Metall. Mater. Trans. A*, 1996, vol. 27A, pp. 2754–64.
21. W. Kurz and D.J. Fisher: *Fundamentals of Solidification*, 4th ed., Trans Tech Publications, Zurich, 1998.
22. H. Combeau, M. Založnik, S. Hans, and P.E. Richy: *Metall. Mater. Trans. B*, 2009, vol. 40B, pp. 289–304.
23. W.D. Bennon and F.P. Incropera: *Int. J. Heat Mass Transfer*, 1987, vol. 30, pp. 2161–70.
24. J. Ni and C. Beckermann: *Metall. Trans. B*, 1991, vol. 22, pp. 349–61.
25. R. Kieffer, G. Jangg, and P. Ettmayer: *Sondermetalle-Metallurgie, Herstellung, Anwendung*, Springer Verlag, Herstellung, 1971, p. 351.
26. P. Lan, Y. Li, J. Zhang, R. Zhang, J. Wang, and H. Zhang: *Extraction and Processing Division Congress*, 2012, pp. 71–78.

27. A. Kermanpur, M. Eskandari, H. Purmohamad, M.A. Soltani, and R. Shateri: *Mater. Des.*, 2010, vol. 31, pp. 1096–1104.
28. H. Jacobi and K. Schwerdtfeger: *Metall. Trans. A*, 1976, vol. 7, pp. 811–20.
29. Z. Chen: Doctoral Thesis, IHEK, RWTH Aachen University, Aachen, Germany, 2015.
30. Z. Chen, P.V. Schweinichen, D. Senk, and A. Lob: “Comparison of As-Cast Structure of Ingots of Different Steel Grades with Regard to Effects of Casting Parameters,” *ICRF 2012*, Aachen, Germany, 2012.
31. H. Preßlinger, S. Ilie, P. Reisinger *et al.*: *ISIJ Int.*, 2006, vol. 46, pp. 1845–51.
32. D. Senk: *Mater. Sci. Forum*, 2010, vols. 638–642, pp. 3628–33.
33. B. Appolaire, V. Albert, H. Combeau, and G. Lesoult: *Acta Mater.*, 1998, vol. 46, pp. 5851–62.
34. S.M. Kharicha, S. Eck, L. Könözy, A. Kharicha, and A. Ludwig: *Int. J. Cast Met. Res.*, 2009, vol. 22, pp. 168–71.
35. S. Eck, M.S. Kharicha, A. Ishmurzin, and A. Ludwig: *Mater. Sci. Eng. A*, 2005, vols. 413–414, pp. 79–84.